Supplementary Material for the Paper "Invariant Filtering for Legged Humanoid Locomotion on a Dynamic Rigid Surface"

Yuan Gao
Ph.D. student
Dept. of Mechanical Engineering
University of Massachusetts Lowell
Lowell, MA 01854, U.S.A.
Email: yuan_gao@student.uml.edu

Chengzhi Yuan
Ph.D., Assistant Professor
Dept. of Mechanical, Industrial
and Systems Engineering
University of Rhode Island
Kingston, RI 02881, U.S.A.
Email: cyuan@uri.edu

Yan Gu *
Ph.D., Associate Professor
School of Mechanical Engineering
Purdue University
West Lafayette, IN 47907, U.S.A.
Email: yan.gu.purdue@gmail.com

NOMENCLATURE

$\boldsymbol{\eta}$	right-invariant error
$\boldsymbol{\omega}$	angular velocity of the robot base frame with respect to (w.r.t.) the base frame
$\boldsymbol{\omega}^{DRS}$	angular velocity of the dynamic rigid surface (DRS) w.r.t. the inertial frame
$\boldsymbol{\theta}$	a vector containing gyroscope and accelerometer biases
$\boldsymbol{\xi}$	log of invariant error
$\boldsymbol{\zeta}$	estimation error od IMU biases
$\mathbf{a}$	linear acceleration of the robot base/IMU w.r.t. the base frame
$\mathbf{b}^{\omega}$	gyroscope bias
$\mathbf{b}^{a}$	accelerometer bias
$\mathbf{h}^{R}$	support-foot orientation w.r.t. the base frame
$\mathbf{h}_c$	forward kinematics from the previous support-foot position to the new support-foot position w.r.t. the base frame
$\mathbf{h}_p$	support-foot position relative to the base w.r.t. the base frame
$\mathbf{p}$	position of the robot base w.r.t. the inertial frame
$\mathbf{p}^{c}$	position of the contact point w.r.t. the inertial frame

*Address all correspondence to this author.

$\mathbf{q}$	joint angle vector
$\mathbf{R}$	orientation of the robot base w.r.t. the inertial frame
$\mathbf{R}^c$	contact frame orientation w.r.t. the base frame
$\mathbf{u}^X$	an input vector of the proposed filter, including the measured contact-point velocity and the raw data returned by the gyroscope, accelerometer, and joint encoders
$\mathbf{v}$	linear velocity of the robot base the inertial frame
$\mathbf{w}$	a noise vector containing noise from gyroscope, accelerometer, contact velocity measurement, gyroscope bias, and accelerometer bias
$\mathbf{w}^\omega$	Gaussian zero-mean noise of gyroscope reading
$\mathbf{w}^a$	Gaussian zero-mean noise of accelerometer reading
$\mathbf{w}^q$	Gaussian zero-mean noise of joint encoder reading
$\mathbf{w}^{b\omega}$	Gaussian zero-mean noise of gyroscope bias
$\mathbf{w}^{ba}$	Gaussian zero-mean noise of accelerometer bias
$\mathbf{w}^{DRS}$	Gaussian zero-mean uncertainty of the known DRS orientation
$\mathbf{w}^X$	a noise vector including noise from the gyroscope, accelerometer, and contact velocity measurement
$\mathbf{X}$	state variables that the proposed filter aims to estimate
$\tilde{(\cdot)}$	measured value of the variable $(\cdot)$
$(\cdot)^\dagger$	values of the state estimate $(\cdot)$ just after a measurement update
$(\cdot)_t$	value of the variable $(\cdot)$ at time t
$(\cdot)_{t^+}$	value of a variable $(\cdot)$ just after the jump at time t
$\bar{(\cdot)}$	estimated value of the variable $(\cdot)$
$\mathbf{R}^{DRS}$	orientation of the dynamic rigid surface (DRS) w.r.t. the inertial frame
$\mathbf{v}^{DRS}$	linear velocity of the DRS w.r.t. the inertial frame
${}^{DRS}\mathbf{p}^c$	position of the contact point w.r.t. the DRS frame

1 BRIEF INTRODUCTION OF INVARIANT FILTERING

The theory of invariant filtering is provided in reference [12] cited in the main paper. The following key concepts of invariant filtering, which are used in this paper, can be found in [12]:

(1) Definitions of invariant errors: Eq. (5) (left invariant) and Eq. (6) (right invariant) in Sec. II-B.
(2) Conditions under which a process model is group affine: Eq. (7) in Sec. II-B.
(3) Log-linear property of invariant errors during the propagation step: Theorem 2 in Sec. II-C.
(4) Invariant observation forms: Eq. (15) (left invariant) and Eq. (22) (right invariant).
(5) Linearized equation of the logarithmic error during the update step: Eqs. (32)-(34) in Sec. III-B.

2 EXPRESSION OF RIGHT-INVARIANT AND LOGARITHMIC ERRORS

The right-invariant error $\boldsymbol{\eta}_t$ is defined as:

$$\boldsymbol{\eta}_t = \bar{\mathbf{X}}_t \mathbf{X}_t^{-1} = \begin{bmatrix} \boldsymbol{\eta}_{R,t} & [\boldsymbol{\eta}_{v,t},\ \boldsymbol{\eta}_{p,t}, \boldsymbol{\eta}_{p^c,t}] \\ \mathbf{0}_{3\times 3} & \mathbf{I}_3 \end{bmatrix}, \tag{1}$$

with the individual terms expressed as:

$$\boldsymbol{\eta}_{R,t} = \bar{\mathbf{R}}_t \mathbf{R}_t^T, \quad \boldsymbol{\eta}_{v,t} = \bar{\mathbf{v}}_t - \bar{\mathbf{R}}_t \mathbf{R}_t^T \mathbf{v}_t, \quad \boldsymbol{\eta}_{p,t} = \bar{\mathbf{p}}_t - \bar{\mathbf{R}}_t \mathbf{R}_t^T \mathbf{p}_t, \quad \text{and} \quad \boldsymbol{\eta}_{p^c,t} = \bar{\mathbf{p}}_t^c - \bar{\mathbf{R}}_t \mathbf{R}_t^T \mathbf{p}_t^c. \tag{2}$$

Denote $\boldsymbol{\xi}_t = \left[(\boldsymbol{\xi}_t^R)^T,\ (\boldsymbol{\xi}_t^v)^T,\ (\boldsymbol{\xi}_t^p)^T,\ (\boldsymbol{\xi}_t^{p^c})^T\right]^T$. Then, the variable $\boldsymbol{\xi}_t^\wedge$ on the Lie algebra $\mathfrak{g}$ is $\boldsymbol{\xi}_t^\wedge = \begin{bmatrix} (\boldsymbol{\xi}_{R,t})_\times & [\boldsymbol{\xi}_{v,t},\ \boldsymbol{\xi}_{p,t},\ \boldsymbol{\xi}_{p^c,t}] \\ \mathbf{0}_{3\times3} & \mathbf{0}_{3\times3} \end{bmatrix}$, where $(\cdot)_\times$ is a skew-symmetric matrix.

3 LINEARIZATION OF CONTINUOUS-PHASE ERROR PROPAGATION EQUATION

To obtain the linearized dynamic of the logarithmic error $\boldsymbol{\xi}_t$, we first apply the chain rule to obtain the time derivatives of the individual terms of the invariant error $\boldsymbol{\eta}_t$ as:

$$\begin{aligned} \dot{\boldsymbol{\eta}}_{R,t} &\approx (\bar{\mathbf{R}}_t(\mathbf{w}_t^\omega - \boldsymbol{\zeta}_t^\omega))_\times, \\ \dot{\boldsymbol{\eta}}_{v,t} &\approx (\mathbf{g})_\times \boldsymbol{\xi}_t^R + (\bar{\mathbf{v}}_t)_\times \bar{\mathbf{R}}_t(\mathbf{w}_t^\omega - \boldsymbol{\zeta}_t^\omega) + \bar{\mathbf{R}}_t(\mathbf{w}_t^a - \boldsymbol{\zeta}_t^a), \\ \dot{\boldsymbol{\eta}}_{p,t} &\approx \boldsymbol{\xi}_t^v + (\bar{\mathbf{p}}_t)_\times \bar{\mathbf{R}}_t(\mathbf{w}_t^\omega - \boldsymbol{\zeta}_t^\omega), \text{ and} \\ \dot{\boldsymbol{\eta}}_{p^c,t} &\approx (\tilde{\mathbf{v}}_t^c)_\times \boldsymbol{\xi}_t^R + (\bar{\mathbf{d}}_t)_\times \bar{\mathbf{R}}_t(\mathbf{w}_t^\omega - \boldsymbol{\zeta}_t^\omega) + \bar{\mathbf{R}}_t \mathbf{w}_t^c, \end{aligned} \tag{3}$$

where $\boldsymbol{\zeta}_t = \left[(\boldsymbol{\zeta}_t^\omega)^T,\ (\boldsymbol{\zeta}_t^a)^T\right]^T$ is the IMU bias error.

Then, we use $\boldsymbol{\eta}_t = \exp(\xi_t) = \text{expm}(\boldsymbol{\xi}_t^\wedge)$ and its first-order approximation $\text{expm}(\boldsymbol{\xi}_t^\wedge) \approx \mathbf{I} + \boldsymbol{\xi}_t^\wedge$ to obtain the following approximations:

$$(\boldsymbol{\xi}_{R,t})_\times \approx \bar{\mathbf{R}}_t \mathbf{R}_t^T - \mathbf{I}_3,\ \boldsymbol{\xi}_{v,t} \approx \bar{\mathbf{v}}_t - \bar{\mathbf{R}}_t \mathbf{R}_t^T \mathbf{v}_t,\ \boldsymbol{\xi}_{p,t} \approx \bar{\mathbf{p}}_t - \bar{\mathbf{R}}_t \mathbf{R}_t^T \mathbf{p}_t, \text{ and } \boldsymbol{\xi}_t^d \approx \bar{\mathbf{d}}_t - \bar{\mathbf{R}}_t \mathbf{R}_t^T \mathbf{d}_t. \tag{4}$$

By combining these equations and applying the chain rule to find the time derivative of $\boldsymbol{\xi}_t$, we obtain the linearized error equation in Eq. (13) of the main manuscript.

In Eq. (13) of the main manuscript, the expression of the adjoint matrix $\mathbf{Ad}_{\mathbf{X}_t}$ is obtained through its basic definition given in Section II (Preliminaries) of the main paper. Its specific expression in Eq. (13) is:

$$\mathbf{Ad}_{\bar{\mathbf{X}}_t} = \begin{bmatrix} \bar{\mathbf{R}}_t & \mathbf{0} & \mathbf{0} & \mathbf{0} \\ (\bar{\mathbf{v}}_t)_\times \bar{\mathbf{R}}_t & \bar{\mathbf{R}}_t & \mathbf{0} & \mathbf{0} \\ (\bar{\mathbf{p}}_t)_\times \bar{\mathbf{R}}_t & \mathbf{0} & \mathbf{R}_t & \mathbf{0} \\ (\bar{\mathbf{p}}_t^c)_\times \bar{\mathbf{R}}_t & \mathbf{0} & \mathbf{0} & \bar{\mathbf{R}}_t \end{bmatrix}, \tag{5}$$

where the matrix $\mathbf{0}$ is a 3×3 zero matrix.

4 LINEARIZATION OF CONTINUOUS-PHASE ERROR UPDATE EQUATION

This section explains the derivation of the linearized update equation for the errors $\boldsymbol{\xi}_{t_n}$ and $\boldsymbol{\zeta}_{t_n}$ in Eq. (18) of the main paper. We will first derive the linearized update equation for $\boldsymbol{\xi}_{t_n}$.

From the estimate update equation in Eq. (17) of the main paper, we have

$$\bar{\mathbf{X}}_{t_n}^{\dagger} = \exp\left(\mathbf{L}_{t_n}^{\xi}\begin{bmatrix}\bar{\mathbf{X}}_{t_n}\mathbf{Y}_{1,t_n} - \mathbf{d}_{1,t_n}\\ \bar{\mathbf{X}}_{t_n}\mathbf{Y}_{2,t_n} - \mathbf{d}_{2,t_n}\end{bmatrix}\right)\bar{\mathbf{X}}_{t_n}. \tag{6}$$

Multiplying $\mathbf{X}_{t_n}^{-1}$ on both sides of Eq. (6) gives:

$$\bar{\mathbf{X}}_{t_n}^{\dagger}\mathbf{X}_{t_n}^{-1} = \exp\left(\mathbf{L}_{t_n}^{\xi}\begin{bmatrix}\bar{\mathbf{X}}_{t_n}\mathbf{Y}_{1,t_n} - \mathbf{d}_{1,t_n}\\ \bar{\mathbf{X}}_{t_n}\mathbf{Y}_{2,t_n} - \mathbf{d}_{2,t_n}\end{bmatrix}\right)\bar{\mathbf{X}}_{t_n}\mathbf{X}_{t_n}^{-1}. \tag{7}$$

Simplifying the above equation yields:

$$\boldsymbol{\eta}_{t_n}^{\dagger} = \exp\left(\mathbf{L}_{t_n}^{\xi}\begin{bmatrix}\boldsymbol{\eta}_{t_n}\mathbf{d}_{1,t_n} + \bar{\mathbf{X}}_{t_n}\begin{bmatrix}\mathbf{V}_{1,t_n}\\ \mathbf{0}_{3\times1}\end{bmatrix} - \mathbf{d}_{1,t_n}\\ \boldsymbol{\eta}_{t_n}\mathbf{d}_{2,t_n} + \bar{\mathbf{X}}_{t_n}\begin{bmatrix}\frac{\partial\mathbf{h}_p}{\partial\mathbf{q}}(\mathbf{q}_{t_n})\mathbf{w}_{t_n}^{q}\\ \mathbf{0}_{3\times1}\end{bmatrix} - \mathbf{d}_{2,t_n}\end{bmatrix}\right)\boldsymbol{\eta}_{t_n}. \tag{8}$$

By utilizing the approximations $\boldsymbol{\eta}_{t_n} \approx \mathbf{I} + \boldsymbol{\xi}_{t_n}^{\wedge}$ and $\exp(\mathbf{a}) \approx \mathbf{I} + \mathbf{a}^{\wedge}$ where $\mathbf{a}$ is the vector inside the parentheses of Eq. (8), and by neglecting higher-order terms, we obtain:

$$\begin{aligned}
\boldsymbol{\xi}_{t_n}^{\dagger} &\approx \boldsymbol{\xi}_{t_n} + \mathbf{L}_{t_n}^{\xi}\begin{bmatrix}\boldsymbol{\xi}_{t_n}^{\wedge}\mathbf{d}_{1,t_n} + \mathbf{X}_{t_n}\begin{bmatrix}\mathbf{V}_{1,t_n}\\ \mathbf{0}_{3\times1}\end{bmatrix}\\ \boldsymbol{\xi}_{t_n}^{\wedge}\mathbf{d}_{2,t_n} + \mathbf{X}_{t_n}\begin{bmatrix}\frac{\partial\mathbf{h}_p}{\partial\mathbf{q}}(\mathbf{q}_{t_n})\mathbf{w}_{t_n}^{q}\\ \mathbf{0}_{3\times1}\end{bmatrix}\end{bmatrix}\\
&= \boldsymbol{\xi}_{t_n} - \mathbf{L}_{t_n}^{\xi}\begin{bmatrix}\tilde{\mathbf{H}}_{1,t_n}\boldsymbol{\xi}_{t_n}\\ \tilde{\mathbf{H}}_{2,t_n}\boldsymbol{\xi}_{t_n}\end{bmatrix} + \mathbf{L}_{t_n}^{\xi}\begin{bmatrix}\begin{bmatrix}\mathbf{V}_{1,t_n}\\ \mathbf{0}_{3\times1}\end{bmatrix}\\ \begin{bmatrix}\frac{\partial\mathbf{h}_p}{\partial\mathbf{q}}(\mathbf{q}_{t_n})\mathbf{w}_{t_n}^{q}\\ \mathbf{0}_{3\times1}\end{bmatrix}\end{bmatrix}\\
&= \boldsymbol{\xi}_{t_n} - \mathbf{L}_{t_n}^{\xi}\mathbf{H}_{t_n}\begin{bmatrix}\boldsymbol{\xi}_{t_n}\\ \boldsymbol{\zeta}_{t_n}\end{bmatrix} + \mathbf{L}_{t_n}^{\xi}\begin{bmatrix}\begin{bmatrix}\mathbf{V}_{1,t_n}\\ \mathbf{0}_{3\times1}\end{bmatrix}\\ \begin{bmatrix}\frac{\partial\mathbf{h}_p}{\partial\mathbf{q}}(\mathbf{q}_{t_n})\mathbf{w}_{t_n}^{q}\\ \mathbf{0}_{3\times1}\end{bmatrix}\end{bmatrix}\\
&= \boldsymbol{\xi}_{t_n} - \mathbf{L}_{t_n}^{\xi}\mathbf{H}_{t_n}\begin{bmatrix}\boldsymbol{\xi}_{t_n}\\ \boldsymbol{\zeta}_{t_n}\end{bmatrix} + \mathbf{L}_{t_n}^{\xi}\begin{bmatrix}\begin{bmatrix}\boldsymbol{\eta}_{t_n}(\tilde{\mathbf{R}}_{t_n}^{DRS}\begin{bmatrix}0 & 0 & 1\end{bmatrix}^T)_{\times}\mathbf{w}_{t_n}^{DRS} + \bar{\mathbf{R}}_{t_n}\frac{\partial\mathbf{h}_{R,3}}{\partial\mathbf{q}}(\tilde{\mathbf{q}}_{t_n})\\ \mathbf{0}_{3\times1}\end{bmatrix}\\ \begin{bmatrix}\bar{\mathbf{R}}_{t_n}\frac{\partial\mathbf{h}_p}{\partial\mathbf{q}}(\tilde{\mathbf{q}}_{t_n})\\ \mathbf{0}_{3\times1}\end{bmatrix}\end{bmatrix}.
\end{aligned} \tag{9}$$

As $\boldsymbol{\eta}_{t_n}$ and $\mathbf{w}_{t_n}^{DRS}$ are small quantities, their product can be ignored. Thus, we have:

$$\boldsymbol{\xi}_{t_n}^{\dagger} \approx \boldsymbol{\xi}_{t_n} - \mathbf{L}_{t_n}^{\xi}\mathbf{H}_{t_n}\begin{bmatrix}\boldsymbol{\xi}_{t_n}\\ \boldsymbol{\zeta}_{t_n}\end{bmatrix} + \mathbf{L}_{t_n}^{\xi}\begin{bmatrix}\begin{bmatrix}\bar{\mathbf{R}}_{t_n}\frac{\partial\mathbf{h}_{R,3}}{\partial\mathbf{q}}(\tilde{\mathbf{q}}_{t_n})\\ \mathbf{0}_{3\times1}\end{bmatrix}\\ \begin{bmatrix}\bar{\mathbf{R}}_{t_n}\frac{\partial\mathbf{h}_p}{\partial\mathbf{q}}(\tilde{\mathbf{q}}_{t_n})\\ \mathbf{0}_{3\times1}\end{bmatrix}\end{bmatrix}. \tag{10}$$

Next, we will derive the linearized update equation for $\boldsymbol{\zeta}_{t_n}$. From the definition of $\boldsymbol{\zeta}_t$, we know:

$$\boldsymbol{\zeta}_{t_n}^{\dagger} = \bar{\boldsymbol{\theta}}_{t_n}^{\dagger} - \boldsymbol{\theta}_{t_n}. \tag{11}$$

Also, from the estimate update equation in Eq. (17) of the main paper, we have:

$$\bar{\boldsymbol{\theta}}_{t_n}^{\dagger} = \bar{\boldsymbol{\theta}}_{t_n} + \mathbf{L}_{t_n}^{\zeta} \left(\begin{bmatrix} \bar{\mathbf{X}}_{t_n} \mathbf{Y}_{1,t_n} - \mathbf{d}_{1,t_n} \\ \bar{\mathbf{X}}_{t_n} \mathbf{Y}_{2,t_n} - \mathbf{d}_{2,t_n} \end{bmatrix} \right). \tag{12}$$

Combining Eqs. (11) and (12) yields:

$$\boldsymbol{\zeta}_{t_n}^{\dagger} = \boldsymbol{\zeta}_{t_n} + \mathbf{L}_{t_n}^{\zeta} \left(\begin{bmatrix} \boldsymbol{\eta}_{t_n} \mathbf{d}_{1,t_n} - \mathbf{d}_{1,t_n} + \bar{\mathbf{X}}_{t_n} \begin{bmatrix} \mathbf{V}_{1,t_n} \\ \mathbf{0}_{3\times 1} \end{bmatrix} \\ \boldsymbol{\eta}_{t_n} \mathbf{d}_{2,t_n} - \mathbf{d}_{2,t_n} + \bar{\mathbf{X}}_{t_n} \begin{bmatrix} \frac{\partial \mathbf{h}_p}{\partial \mathbf{q}}(\mathbf{q}_{t_n}) \mathbf{w}_{t_n}^{q} \\ \mathbf{0}_{3\times 1} \end{bmatrix} \end{bmatrix} \right). \tag{13}$$

By utilizing the approximation $\boldsymbol{\eta}_{t_n} \approx \mathbf{I} + \boldsymbol{\xi}_{t_n}^{\wedge}$ and neglecting higher-order terms, we obtain:

$$\begin{aligned}
\boldsymbol{\zeta}_{t_n}^{\dagger} &\approx \boldsymbol{\zeta}_{t_n} + \mathbf{L}_{t_n}^{\zeta} \begin{bmatrix} \boldsymbol{\xi}_{t_n}^{\wedge} \mathbf{d}_{1,t_n} + \bar{\mathbf{X}}_{t_n} \begin{bmatrix} \mathbf{V}_{1,t_n} \\ \mathbf{0}_{3\times 1} \end{bmatrix} \\ \boldsymbol{\xi}_{t_n}^{\wedge} \mathbf{d}_{2,t_n} + \bar{\mathbf{X}}_{t_n} \begin{bmatrix} \frac{\partial \mathbf{h}_p}{\partial \mathbf{q}}(\mathbf{q}_{t_n}) \mathbf{w}_{t_n}^{q} \\ \mathbf{0}_{3\times 1} \end{bmatrix} \end{bmatrix} \\
&= \boldsymbol{\zeta}_{t_n} + \mathbf{L}_{t_n}^{\zeta} \begin{bmatrix} -\tilde{\mathbf{H}}_{1,t_n} \boldsymbol{\xi}_{t_n} + \bar{\mathbf{X}}_{t_n} \begin{bmatrix} \mathbf{V}_{1,t_n} \\ \mathbf{0}_{3\times 1} \end{bmatrix} \\ -\tilde{\mathbf{H}}_{2,t_n} \boldsymbol{\xi}_{t_n} + \bar{\mathbf{X}}_{t_n} \begin{bmatrix} \frac{\partial \mathbf{h}_p}{\partial \mathbf{q}}(\mathbf{q}_{t_n}) \mathbf{w}_{t_n}^{q} \\ \mathbf{0}_{3\times 1} \end{bmatrix} \end{bmatrix} \\
&= \boldsymbol{\zeta}_{t_n} - \mathbf{L}_{t_n}^{\zeta} \begin{bmatrix} \tilde{\mathbf{H}}_{1,t_n} \boldsymbol{\xi}_{t_n} \\ \tilde{\mathbf{H}}_{2,t_n} \boldsymbol{\xi}_{t_n} \end{bmatrix} + \mathbf{L}_{t_n}^{\zeta} \begin{bmatrix} \begin{bmatrix} \boldsymbol{\eta}_{t_n} (\tilde{\mathbf{R}}_{t_n}^{DRS} \begin{bmatrix} 0 & 0 & 1 \end{bmatrix}^T)_{\times} \mathbf{w}_{t_n}^{DRS} + \bar{\mathbf{R}}_{t_n} \frac{\partial \mathbf{h}_{R,3}}{\partial \mathbf{q}}(\mathbf{q}_{t_n}) \\ \mathbf{0}_{3\times 1} \end{bmatrix} \\ \begin{bmatrix} \bar{\mathbf{R}}_{t_n} \frac{\partial \mathbf{h}_p}{\partial \mathbf{q}}(\mathbf{q}_{t_n}) \\ \mathbf{0}_{3\times 1} \end{bmatrix} \end{bmatrix} \\
&\approx \boldsymbol{\zeta}_{t_n} - \mathbf{L}_{t_n}^{\zeta} \begin{bmatrix} \tilde{\mathbf{H}}_{1,t_n} \boldsymbol{\xi}_{t_n} \\ \tilde{\mathbf{H}}_{2,t_n} \boldsymbol{\xi}_{t_n} \end{bmatrix} + \mathbf{L}_{t_n}^{\zeta} \begin{bmatrix} \begin{bmatrix} \bar{\mathbf{R}}_{t_n} \frac{\partial \mathbf{h}_{R,3}}{\partial \mathbf{q}}(\mathbf{q}_{t_n}) \\ \mathbf{0}_{3\times 1} \end{bmatrix} \\ \begin{bmatrix} \bar{\mathbf{R}}_{t_n} \frac{\partial \mathbf{h}_p}{\partial \mathbf{q}}(\mathbf{q}_{t_n}) \\ \mathbf{0}_{3\times 1} \end{bmatrix} \end{bmatrix}.
\end{aligned} \tag{14}$$

Arranging Eqs.(10) and (14) into the matrix forms gives:

$$\begin{bmatrix} \boldsymbol{\xi}_{t_n}^{\dagger} \\ \boldsymbol{\zeta}_{t_n}^{\dagger} \end{bmatrix} = (\mathbf{I} - \mathbf{L}_{t_n} \mathbf{H}_{t_n}) \begin{bmatrix} \boldsymbol{\xi}_{t_n} \\ \boldsymbol{\zeta}_{t_n} \end{bmatrix} + \mathbf{L}_{t_n} \begin{bmatrix} \bar{\mathbf{R}}_{t_n} \frac{\partial \mathbf{h}_{R,3}}{\partial \mathbf{q}}(\tilde{\mathbf{q}}_{t_n}) \\ \mathbf{0}_{3\times 1} \\ \bar{\mathbf{R}}_{t_n} \frac{\partial \mathbf{h}_p}{\partial \mathbf{q}}(\tilde{\mathbf{q}}_{t_n}) \\ \mathbf{0}_{3\times 1} \end{bmatrix} \mathbf{w}_{t_n}^{q}. \tag{15}$$

5 PROPOSED FILTER ALGORITHM

The complete algorithm of the proposed right-invariant extended Kalman filter (right-InEKF) is summarized in Algorithm 1.

Algorithm 1: Proposed Right InEKF for Hybrid Models of DRS Locomotion

Initialize: i) $\bar{\mathbf{X}}_{t_0} \in SE3(3)$; ii) $\mathbf{P}_{t_0}$ is symmetric, positive-definite.
while *True* **do**
  if *a foot landing (i.e., a jump) is detected* **then**
    Propagation at a jump
    $\bar{\mathbf{X}}_{t^+} = \boldsymbol{\Delta}_{u_t}(\bar{\mathbf{X}}_t)$, $\bar{\boldsymbol{\theta}}_{t^+} = \bar{\boldsymbol{\theta}}_t$, $\mathbf{P}_{t^+} = \mathbf{P}_t + \bar{\mathbf{Q}}_t^{\Delta}$
  else
    Propagation for continuous phases
    $\dot{\bar{\mathbf{X}}}_t = \mathbf{f}_{u_t}(\bar{\mathbf{X}}_t, \bar{\boldsymbol{\theta}}_t)$, $\dot{\bar{\boldsymbol{\theta}}}_t = \mathbf{0}$, $\dot{\mathbf{P}}_t = \mathbf{A}_t\mathbf{P}_t + \mathbf{P}_t\mathbf{A}_t^T + \bar{\mathbf{Q}}_t$
    Update for continuous phases
    $\mathbf{S}_{t_n} = \mathbf{H}_{t_n}\mathbf{P}_{t_n}\mathbf{H}_{t_n}^T + \bar{\mathbf{N}}_{t_n}$
    $\mathbf{z}_{tn} = \left[(\bar{\mathbf{X}}_{t_n}\mathbf{Y}_{1,t_n} - \mathbf{d}_{1,t_n})^T,\ (\bar{\mathbf{X}}_{t_n}\mathbf{Y}_{2,t_n} - \mathbf{d}_{2,t_n})^T\right]^T$
    $\mathbf{L}_{t_n} = \left[(\mathbf{L}_{t_n}^{\xi})^T,\ (\mathbf{L}_{t_n}^{\zeta})^T\right]^T = \mathbf{P}_{t_n}\mathbf{H}_{t_n}^T\mathbf{S}_{t_n}^{-1}$
    $\mathbf{P}_{t_n}^{\dagger} = (\mathbf{I} - \mathbf{L}_{t_n}\mathbf{H}_{t_n})\mathbf{P}_{t_n}$
    $\bar{\mathbf{X}}_{t_n}^{\dagger} = \exp\left(\mathbf{L}_{t_n}^{\xi}\mathbf{z}_{t_n}\right)\bar{\mathbf{X}}_{t_n}$
    $\bar{\boldsymbol{\theta}}_{t_n}^{\dagger} = \bar{\boldsymbol{\theta}}_{t_n} + \mathbf{L}_{t_n}^{\zeta}\mathbf{z}_{t_n}$
  end
end

6 MATRICES USED IN OBSERVABILITY ANALYSIS

In the observability analysis in the main paper (Section V-A), the updated expressions of the matrices $\mathbf{A}_t$ and $\mathbf{H}_t$ in the absence of IMU biases are:

$$\mathbf{A}_t = \begin{bmatrix} \mathbf{0}_{3\times3} & \mathbf{0}_{3\times3} & \mathbf{0}_{3\times3} & \mathbf{0}_{3\times3} \\ (\mathbf{g})_\times & \mathbf{0}_{3\times3} & \mathbf{0}_{3\times3} & \mathbf{0}_{3\times3} \\ \mathbf{0}_{3\times3} & \mathbf{I}_3 & \mathbf{0}_{3\times3} & \mathbf{0}_{3\times3} \\ (\tilde{\mathbf{v}}_t^c)_\times & \mathbf{0}_{3\times3} & \mathbf{0}_{3\times3} & \mathbf{0}_{3\times3} \\ \mathbf{0}_{6\times3} & \mathbf{0}_{6\times3} & \mathbf{0}_{6\times3} & \mathbf{0}_{6\times3} \end{bmatrix} \quad \text{and} \quad \mathbf{H}_t = \begin{bmatrix} \mathbf{H}_{1,t} \\ \mathbf{H}_{2,t} \end{bmatrix} = \begin{bmatrix} (\mathbf{R}_t^{DRS}\ [0,0,1]^T)_\times & \mathbf{0}_{3\times3} & \mathbf{0}_{3\times3} & \mathbf{0}_{3\times3} \\ \mathbf{0}_{3\times3} & \mathbf{0}_{3\times3} & \mathbf{0}_{3\times3} & \mathbf{0}_{3\times3} \\ \mathbf{0}_{3\times3} & \mathbf{0}_{3\times3} & \mathbf{I}_3 & \mathbf{I}_3 \\ \mathbf{0}_{3\times3} & \mathbf{0}_{3\times3} & \mathbf{0}_{3\times3} & \mathbf{0}_{3\times3} \end{bmatrix}. \tag{16}$$

In Eq. (20) of the observability analysis in the main paper (Section V-A), the discrete state transition matrix $\boldsymbol{\Phi}$ is given by:

$$\boldsymbol{\Phi} = \text{expm}(\mathbf{A}_t\Delta t) = \begin{bmatrix} \mathbf{I}_3 & \mathbf{0}_{3\times3} & \mathbf{0}_{3\times3} & \mathbf{0}_{3\times3} \\ (\mathbf{g})_\times\Delta t & \mathbf{I}_3 & \mathbf{0}_{3\times3} & \mathbf{0}_{3\times3} \\ \frac{1}{2}(\mathbf{g})_\times\Delta t^2 & \mathbf{I}_3\Delta t & \mathbf{I}_3 & \mathbf{0}_{3\times3} \\ (\tilde{\mathbf{v}}_t^c)_\times\Delta t & \mathbf{0}_{3\times3} & \mathbf{0}_{3\times3} & \mathbf{I}_3 \end{bmatrix}, \tag{17}$$

where Δt is the duration of one propagation step.

7 CONTACT POINT VELOCITY SENSING

This section explains how to obtain the contact point velocity in the world frame, $\mathbf{v}_t^c$, which is briefly summarized in Section VI-B of the main paper. For brevity, we drop the time t from the subscripts of all variables in this section.

We first obtain the 3-D contact point position in the DRS frame, ${}^{DRS}\mathbf{p}^c := [{}^{DRS}p_x^c,\ {}^{DRS}p_y^c,\ {}^{DRS}p_z^c]^T$ (see Fig. 1 in the main paper), by using the RGB-D camera to track features of the ArUco markers in the camera images, as summarized in Fig. 6 of the main manuscript. The detailed procedure of this step is:

(a) Obtain the pixel coordinates $(x_{marker,i}^{img}, y_{marker,i}^{img})$ of the ith corner for all markers in the image frame;
(b) Extract the depth value $d_{mark,i}^{img}$ of the pixel $(x_{marker,i}^{img}, y_{marker,i}^{img})$;
(c) Apply deprojection [1] to obtain the 3-D coordinates $(x_{marker,i}^{cam}, y_{marker,i}^{cam}, z_{marker,i}^{cam})$ of the ith corner with respect to (w.r.t.) the camera frame;
(d) With all the detected corners of the markers and their corresponding known position w.r.t. the treadmill, apply Kabsch algorithm [2] to obtain the optimal estimated camera orientation ${}^{DRS}\tilde{\mathbf{R}}^{cam}$ and position ${}^{DRS}\tilde{\mathbf{p}}^{cam}$ of the RGB-D camera w.r.t. the treadmill frame.

Second, we compute the surface-foot contact point position w.r.t. the treadmill frame ${}^{DRS}\mathbf{p}^c := [{}^{DRS}p_x^c,\ {}^{DRS}p_y^c,\ {}^{DRS}p_z^c]^T$ through forward kinematics $\mathbf{h}_{cam}(\mathbf{q})$. Here, $\mathbf{h}_{cam}(\mathbf{q})$ is the contact point position in the camera frame. Let ${}^{DRS}\tilde{\mathbf{p}}^c = [{}^{DRS}\tilde{p}_x^c,\ {}^{DRS}\tilde{p}_y^c,\ {}^{DRS}\tilde{p}_z^c]^T$ denote the computed value of ${}^{DRS}\mathbf{p}^c$. Then we have ${}^{DRS}\tilde{\mathbf{p}}^c = {}^{DRS}\tilde{\mathbf{R}}^{cam}\mathbf{h}_{cam}(\tilde{\mathbf{q}}) + {}^{DRS}\tilde{\mathbf{p}}^{cam}$.

Finally, we estimate the contact point velocity $\mathbf{v}^c$ as $\tilde{\mathbf{v}}^c = [\tilde{v}_x^c, \tilde{v}_y^c, \tilde{v}_z^c]^T$ based on the known treadmill pitch angle $\tilde{\theta}^{DRS}$ and velocity $\dot{\tilde{\theta}}^{DRS}$ and forward kinematics:

$$\|\tilde{\mathbf{v}}^c\| = (\dot{\tilde{\theta}}^{DRS})({}^{DRS}\tilde{p}_x^c), \quad \tilde{v}_x^c = \|\tilde{\mathbf{v}}^c\| \sin(\tilde{\theta}^{DRS}), \quad \tilde{v}_y^c = 0, \quad \text{and} \quad \tilde{v}_z^c = \|\tilde{\mathbf{v}}^c\| \cos(\tilde{\theta}^{DRS}). \tag{18}$$

8 DESCRIPTIONS OF FIGURES

8.1 Filter Performance under Different DRS and Robot Movements for Cases B and C

Figure 1 displays the comparison results of the two filters (i.e., the proposed InEKF-DRS and the existing InEKF-SRS) under Cases B and C. The interpretation of the results is available in Section VI-F of the main manuscript, which is quoted as follows:

“ Figures 1-a) and 1-b) in supplementary material respectively show the estimation results of the two filters under Case B (where the treadmill motion is different from Case A) and Case C (where the robot stands on the treadmill instead of walking as in Case A). The plots show that the performance comparison of the two filters under Cases B and C are similar to Case A shown in Fig. 8-a), in terms of convergence rate, yaw observability, and accuracy. This indicates the effectiveness of the proposed InEKF-DRS in handling different DRS and robot movements.

Comparing the convergence rate of the yaw estimate under the proposed InEKF-DRS in Cases A-C, we notice that the yaw estimate in Case C converges faster than Cases A and B. In Case C, the treadmill remains horizontal for the first 10 sec, during which the yaw estimate does not converge. Yet, once the treadmill begins to rock at $t = 10$ sec, the yaw estimate converges close to the ground truth within 1 sec, whereas it takes about 3 sec for the yaw estimate to enter into a similar neighborhood under Cases A and B. This might be due to the fact that in Case C, by the

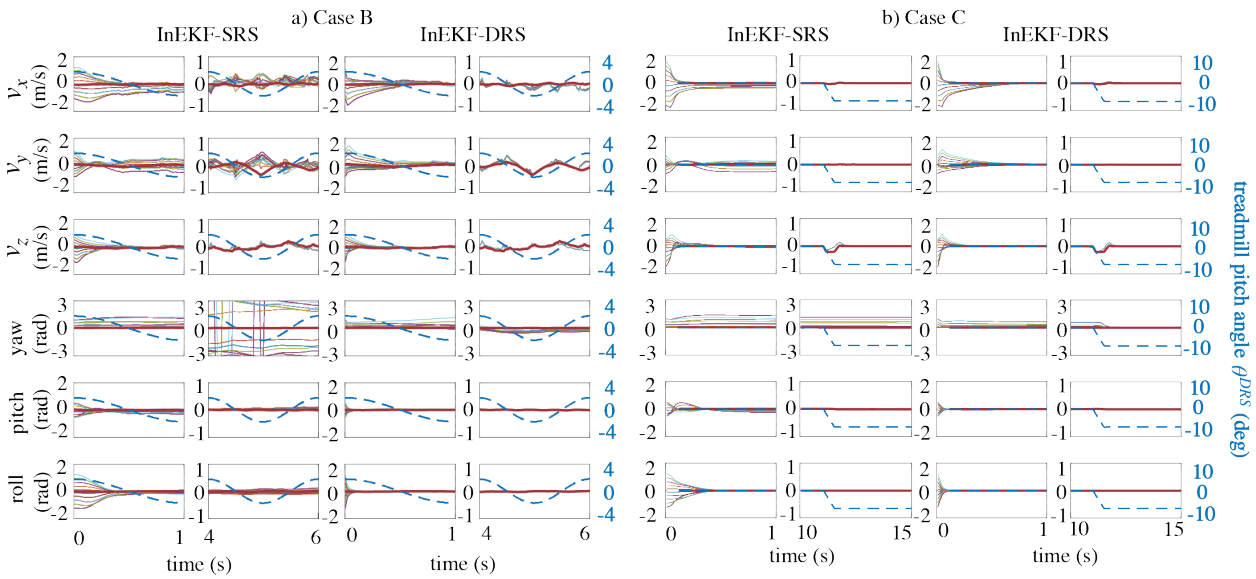

Fig. 1. Base velocity and orientation estimation results of the two filters, InEKF-DRS (proposed) and InEKF-SRS, for Cases B and C. The thin, solid and thick, solid lines are the estimates and ground truth of the base velocity and orientation. The blue, dashed lines are the treadmill orientation profile.

time the treadmill begins to pitch, the estimates of the rest observable state are already sufficiently accurate, making the correction of the yaw error faster than Cases A and B. ”

8.2 Additional Validation Results on Robustness

Figures 2-5 show the results of our proposed filter under Cases A-D for longer periods (10-30 sec). These results demonstrate filter performance similar to previously discussed plots (i.e., Fig. 8 in the main paper and Fig. 1 in the supplementary material), in terms of convergence rate, accuracy, and state observability.

In Figs. 2 and 5, there are a few bumps (around $t = 10$ sec) in the velocity estimate in x-direction as well as in the yaw angle estimate. Around $t = 10$ sec, the robot steps onto the elevated edges of the treadmill due to its temporary loss of balance in response to the significant treadmill movement. The robot regained its balance after a few walking steps, during which the robot's support foot and the surface have relative movement and their normal vectors are not precisely aligned. This robot behavior can be clearly observed in the video submission for Cases A and D. Since the foot-surface contact during this transient process is not accurately captured by the process and measurement models, the estimates temporarily diverge from the ground truth, showing the few “bumps” in Figs. 2 and 5. Still, shortly after the robot regains its balance and resumes a relatively secured foot contact with the treadmill at around $t = 12$ sec, the velocity and yaw estimates converge back to close to the ground truth, which demonstrates the robustness of our proposed filter.

8.2 Additional Validation Results on Robustness

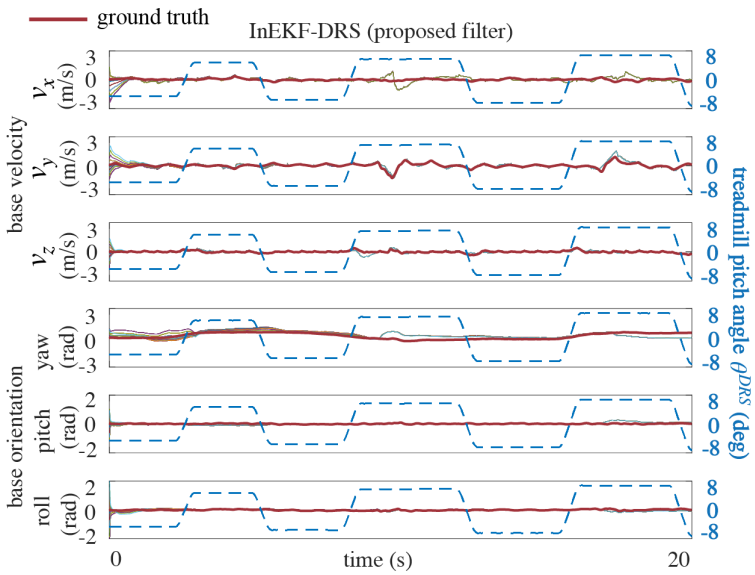

Fig. 2. Base velocity and orientation estimation results of the two filters, InEKF-DRS (proposed) and InEKF-SRS, for Case A. The thin, solid and thick, solid lines are the estimates and ground truth of the base velocity and orientation. The blue, dashed lines are the treadmill orientation profile.

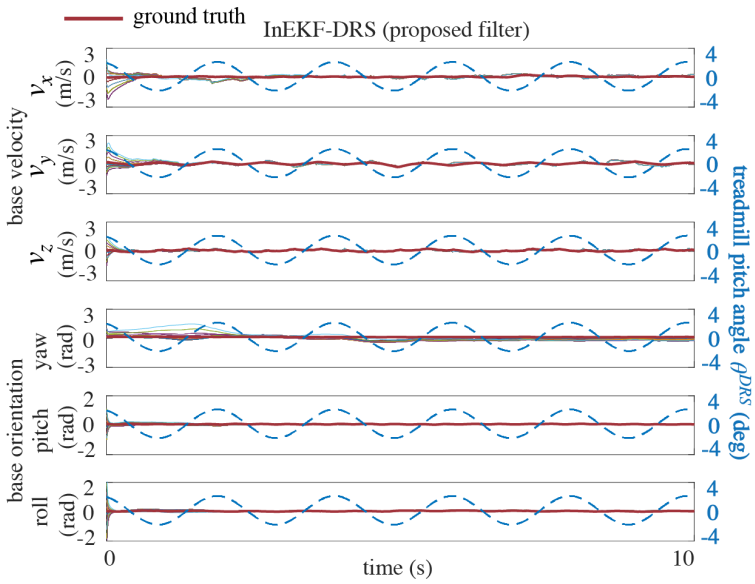

Fig. 3. Base velocity and orientation estimation results of the proposed filer, InEKF-DRS, for Case B. The thin, solid and thick, solid lines are the estimates and ground truth of the base velocity and orientation. The blue, dashed lines are the treadmill orientation profile.

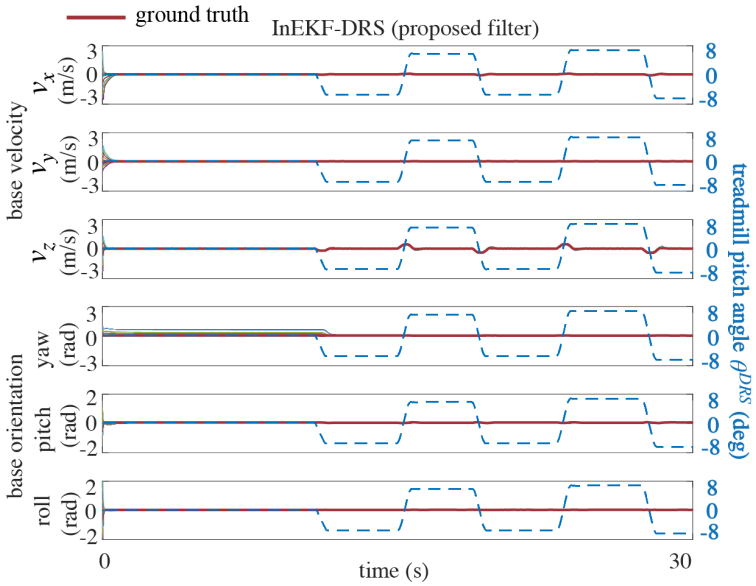

Fig. 4. Base velocity and orientation estimation results of the proposed filer, InEKF-DRS, for Case C. The thin, solid and thick, solid lines are the estimates and ground truth of the base velocity and orientation. The blue, dashed lines are the treadmill orientation profile.

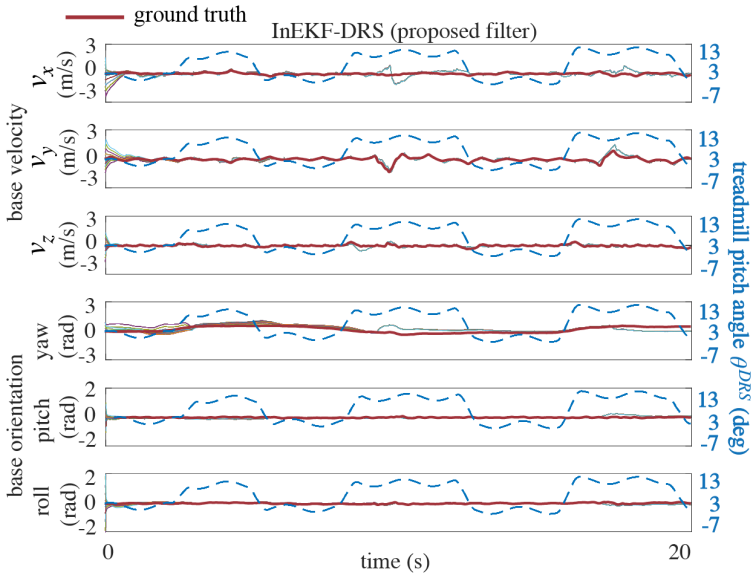

Fig. 5. Base velocity and orientation estimation results of the proposed filer, InEKF-DRS, for Case D. The thin, solid and thick, solid lines are the estimates and ground truth of the base velocity and orientation. The blue, dashed lines are the treadmill orientation profile.

8.3 Comparison with EKF-DRS

To further validate the strength of our proposed filter (InEKF-DRS) beyond the comparison with InEKF-SRS as discussed in the main paper, we augment a state-of-the-art extended Kalman filter (EKF) [3] to explicitly address DRS motions, which we call "EKF-DRS," and compare the performance of our InEKF-DRS over the EKF-DRS under various initial estimation errors, surface movements, and robot motions.

8.3.1 Process and measurement models

The previous EKF-based filter design [3] for legged robot locomotion on stationary surfaces shares several key features with the proposed filter (and several other existing InEKFs cited in the main paper). The state variables include the position, linear velocity, and orientation of the robot's base/IMU with respect to (w.r.t.) the world frame as well as the contact point position in the world frame. The process model uses the simple IMU motion dynamics and considers the dynamics of the contact point position. The measurement model is a 3-D position vector represented through the forward kinematic chain starting at the origin of the base frame and ending at the contact point.

To augment the existing EKF design to address surface motions, we explicitly add the surface movement in the dynamics of the contact point. This is the only augmentation performed here.

The resulting process model of the EKF-DRS at time t is:

$$\begin{aligned} \frac{d}{dt}\mathbf{p}_t = \mathbf{v}_t, \quad \frac{d}{dt}\mathbf{v}_t = \mathbf{R}_t(\tilde{\mathbf{a}}_t - \mathbf{b}_t^a + \boldsymbol{w}_t^a) + \mathbf{g}, \quad \frac{d}{dt}\mathbf{d}_t = \tilde{\mathbf{v}}_t^d + \boldsymbol{w}_t^d, \\ \frac{d}{dt}\mathbf{b}_t^a = \mathbf{w}_t^{ba}, \quad \frac{d}{dt}\mathbf{b}_t^\omega = \mathbf{w}_t^{b\omega}, \\ \frac{d}{dt}\mathbf{q}_t^b = \mathbf{q}_t^b \odot \exp_q(\frac{1}{2}(\tilde{\boldsymbol{\omega}}_t - \mathbf{b}_t^\omega + \mathbf{w}_t^g)). \end{aligned} \tag{19}$$

Here, all the vectors are defined in Section III of the main paper as well as in the nomenclature table at the beginning of this supplementary file, except for the vector $\mathbf{q}_t^b$. The vector $\mathbf{q}_t^b$ is a quaternion used to represent the base orientation. The operator $\odot$ is the quaternion multiplication operator and $\exp_q$ is the quaternion exponential map.

The measurement model is the support foot position w.r.t. the base frame:

$$\mathbf{h}_p(\tilde{\mathbf{q}}_t) = \mathbf{R}_t^T(\mathbf{d}_t - \mathbf{p}_t) + \mathbf{J}_p(\tilde{\mathbf{q}}_t)\boldsymbol{w}_t^q. \tag{20}$$

With such an augmentation, the major difference between the proposed InEKF-DRS and the augmented EKF-DRS is two-fold. First, the proposed InEKF-DRS is a filter designed on the matrix Lie group and enjoys the fundamental benefits of the group-affine process model (without IMU biases) and right-invariant observations, whereas the augmented EKF-DRS is formed on the usual Euclidean space. As discussed in the main paper, thanks to these fundamental properties, the deterministic logarithmic error dynamics during the propagation step is exactly linear and independent of the state trajectories for the proposed filter (without IMU biases). Also, the deterministic, linearized dynamics of the logarithmic error during the update step is independent of the state trajectories (without IMU biases). For these reasons, the proposed filter can achieve rapid error convergence and high estimation accuracy even under large initial errors as discussed in the

main paper. In contrast, the filter gain of the EKF-DRS is computed based on the linearization of error dynamics performed at the state estimate, and thus the filter may not be effective under large errors.

Second, the proposed InEKF-DRS contains two measurement models while the EKF-DRS only has one of them. The additional measurement model that the InEKF-DRS possesses is the proposed orientation-based measurement model built upon the alignment of normal vectors between the surface and the foot. As shown in the main paper, this observation helps render the base yaw angle observable when the surface is not horizontal. However, the yaw angle remains unobservable under the EKF-DRS. The observability of the other state variables is the same between the two filters. The effects of these two differences on the filters' performance are explained next.

8.3.2 Comparison results

The covariance setting for the EKF-DRS filter is as same as the proposed InEKF-DRS, which is given in the main paper. The initial value of the estimated covariance matrix $\mathbf{P}$ is an identity matrix under both filters.

As the EKF-DRS diverges more easily compared with the InEKF-DRS in the presence of large initial estimation errors, the initial errors are set to be smaller than those used to compare InEKF-DRS and InEKF-SRS. Specifically, we reduce the range of the initial orientation errors to be $[-0.2, 0.2]$ rad while the initial velocity error range is still $[-1.5, 1.5]$ m/s. Under each of Cases A-D (which are explained in the main paper and correspond to different surface and robot motions), five trials are tested for each filter within these error ranges.

The filtering results are given in Figs. 6-9. The results show that even under the reduced range of initial errors, the EKF-DRS diverges during one out of the five trials in each of the four cases. Also, the yaw angle is indeed unobservable as indicated by the results. In contrast, the proposed InEKF-DRS rapidly drives the state estimates to the ground truth and achieves smaller errors near the steady state. The yaw estimate begins to converge to the ground truth as soon as the surface is no longer horizontal.

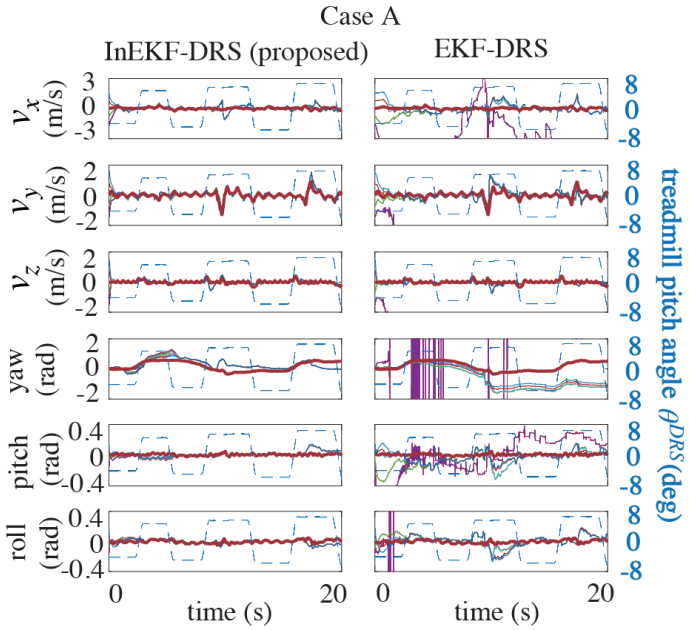

Fig. 6. Base velocity and orientation estimation results of the two filters, InEKF-DRS (proposed) and EKF-DRS, for Case A. The thin, solid and thick, solid lines are the estimates and ground truth of the base velocity and orientation. The blue, dashed lines are the treadmill orientation profile. EKF-DRS has one curve that diverges.

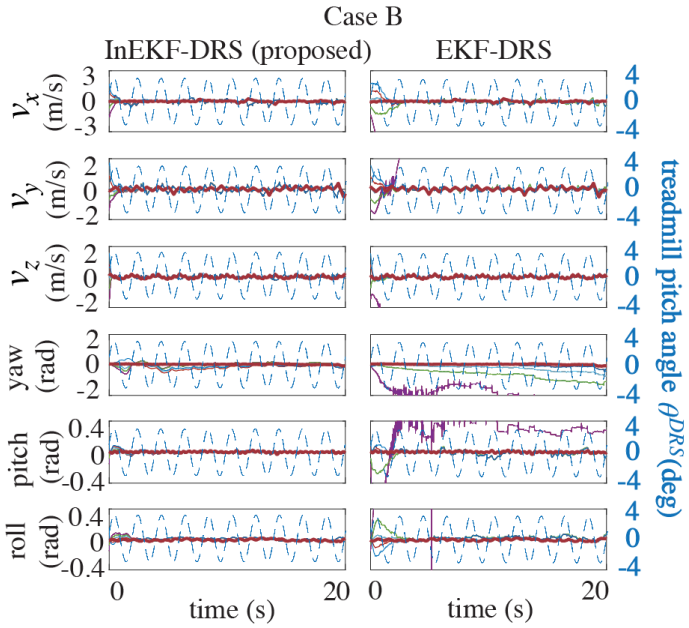

Fig. 7. Base velocity and orientation estimation results of the two filters, InEKF-DRS (proposed) and EKF-DRS, for Case B. The thin, solid and thick, solid lines are the estimates and ground truth of the base velocity and orientation. The blue, dashed lines are the treadmill orientation profile. EKF-DRS has one curve that diverges.

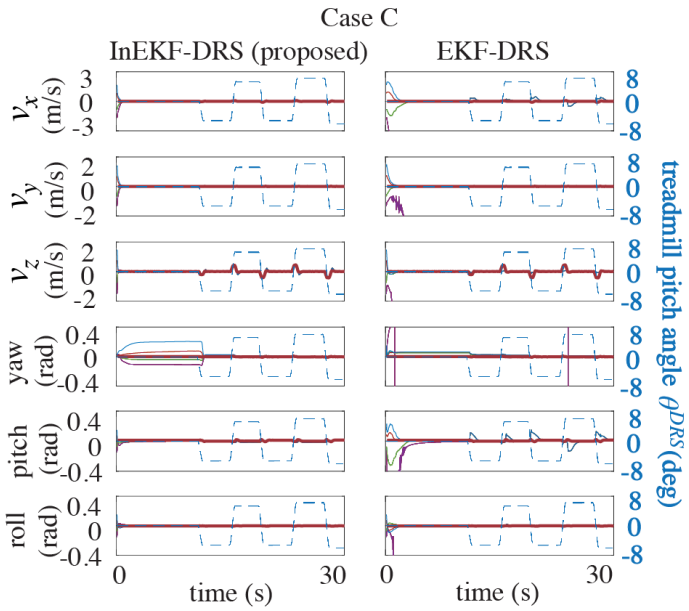

Fig. 8. Base velocity and orientation estimation results of the two filters, InEKF-DRS (proposed) and EKF-DRS, for Case C. The thin, solid and thick, solid lines are the estimates and ground truth of the base velocity and orientation. The blue, dashed lines are the treadmill orientation profile. EKF-DRS has one curve that diverges.

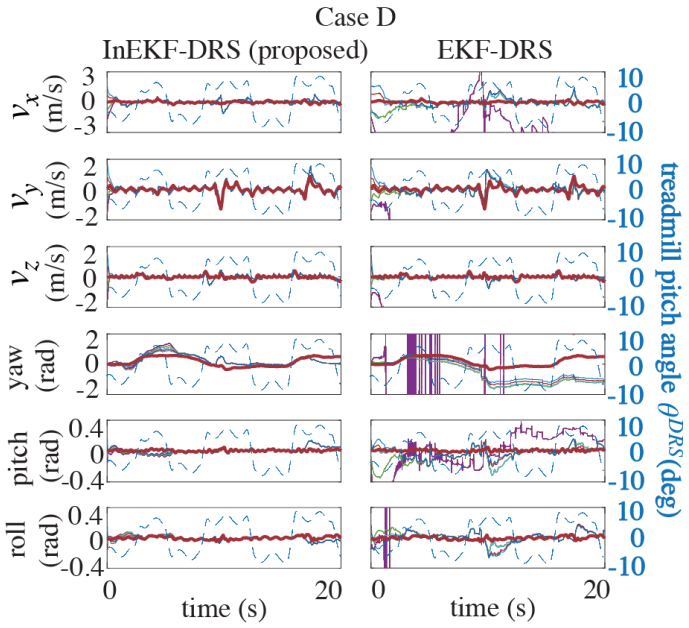

Fig. 9. Base velocity and orientation estimation results of the two filters, InEKF-DRS (proposed) and EKF-DRS, for Case D. The thin, solid and thick, solid lines are the estimates and ground truth of the base velocity and orientation. The blue, dashed lines are the treadmill orientation profile. EKF-DRS has one curve that diverges.

REFERENCES

[1] Intel, Accessed: 2021-08-08. “Realsense sdk”. *https://dev.intelrealsense.com/docs/projection-in-intel-realsense-sdk-20*.

[2] Kabsch, W., 1976. “A solution for the best rotation to relate two sets of vectors”. *Acta Crystallographica Section A: Crystal Physics, Diffraction, Theoretical and General Crystallography,* **32**(5), pp. 922–923.

[3] Bloesch, M., Hutter, M., Hoepflinger, M. A., Leutenegger, S., Gehring, C., Remy, C. D., and Siegwart, R., 2013. “State estimation for legged robots-consistent fusion of leg kinematics and IMU”. *Robotics,* **17**, pp. 17–24.